JMEPEG (2020) 29:8348–8358
https://doi.org/10.1007/s11665-020-05256-0


1059-9495/$19.00

# Effect of Mechanical Milling on the Mechanical, Dry Sliding Wear, and Impact Response of Sintered Nickel Based Superalloy

*Bukola Joseph Babalola, Smith Salifu, and Peter Apata Olubambi*

Submitted: 2 August 2020 / Revised: 14 September 2020 / Accepted: 3 October 2020 / Published online: 2 November 2020

**In this study, effect of mechanical milling on the mechanical, dry sliding wear and impact response of spark plasma sintered Ni-17Cr6.5Co1.2Mo6Al4W7.6Ta superalloy has been investigated. Two nickel-based superalloy were sintered, firstly in their as-received elemental particle sizes, while the matrix, nickel of the second alloy, was milled to 10 h prior blending with other elements and subsequent sintering. The impact response was explored using computational modelling approach via finite element analysis, Abaqus CAE/2019. Results show that the superalloy with the milled nickel powder exhibited better mechanical properties such hardness, elastic modulus, elastic and plastic strain from impact response than the superalloys with unmilled nickel. Sliding wear tests under dry sliding conditions at three different loads of 20, 25 and 30 N revealed that the superalloy with the milled nickel have lower wear rate when compared to the other with unmilled nickel. It was observed that the wear rate reduced unexpectedly at the applied load of 30 N which may be attributed to the continuous formation of tribo-oxide layer from retained wear debris on worn surface.**

**Keywords** hardness, modelling, spark plasma sintering, superalloys, wear

## 1. Introduction

The growing interest in the development of nickel-based superalloy via advanced processing routes since the 1990s has been poised towards enhanced energy production and aerospace engine performance (Ref 1). Nickel-based superalloys are utilized in the high temperature regime of turbines in power plants (Ref 2, 3) marine and aerospace engines (Ref 4) and are suitable replacements for steel components in these environments as a result of their superior mechanical strength retention and excellent corrosion and oxidation resistance properties (Ref 1, 5-7). There have been historical advancement in the development of nickel-based superalloys which have resulted into improvement in the superalloys' performance in service. According to Sommitsch et al. (Ref 8), operating temperature of superalloy increases by the use of investment casting production route in the 1940s, while the reduction in contamination and control of the chemistry and microstructure was achieved via the introduction of vacuum melting in the 1950s. However, these conventional processing routes contribute defects such as poor density, low hardness and strength at relatively elevated temperatures, microstructures with high grain size (Ref 9), which reduces its intrinsic properties and in turn serves as an impediment to perform excellently, while in service. This has necessitated the need for an advanced fabrication technique capable of eliminating defects inherent in conventional processing route with the aim of attaining improved performance in service. Spark plasma sintering (SPS) technique, a novel processing route has become attractive to researchers over the years owing to its capability to produce dense materials at lower sintering temperatures, higher heating rates and reduced holding time when compared to the conventional sintering routes (Ref 10, 11). Its advantages range from ability to retain fine microstructure, elimination of foreign inclusions, relatively shorter processing time (Ref 12, 13), limited grain growth (Ref 14) and easy control of processing parameters among others (Ref 15-17). The combined effect of uniaxial pressure and pulsed electric current with low voltage within the confinement of graphite die were used for the consolidation of powders (Ref 12, 18, 19). Critical properties required for nickel-based superalloys for effective performance in service entails superior mechanical strength, excellent wear properties, high resistance to corrosion and oxidation and stability of phase at elevated temperature (Ref 20-22). These properties can be influenced retrogressively via the adopted processing route which in turn alters the microstructure of a material, owing to the fact that the intrinsic properties of a processed material are influenced by their microstructure (Ref 8). Nickel-based superalloys utilized in the moving sections of engines are faced with aggressive service conditions which bring about impediments such as reduced mechanical strength resulting from wear (Ref 21). In as much relative motion between component's surfaces is unavoidable in engine components, an approach from the manufacturing point of view of these materials to prevent degradation, reduced life span and to clamp down on economic loss is required. Substantial work has been reported on the development and characterization of nickel-based superalloy. Yong Gao and Mingzhuo Zhou (Ref

**Bukola Joseph Babalola** and **Peter Apata Olubambi**, Centre for Nanomechanics and Tribocorrosion, School of Mining, Metallurgy and Chemical Engineering, University of Johannesburg, Johannesburg 2092, South Africa; and **Smith Salifu**, Department of Mechanical and Automation Engineering, Tshwane University of Technology, Pretoria, South Africa. Contact e-mail: beejegs@gmail.com.

23) investigated the mechanical and tribological behaviour of additively manufactured Inconel 625 superalloy via electron beam selective melting. It was reported that a 335 HV hardness value was attained by the alloy, and the excellent wear behaviour of the superalloy was as a result of the development of steady tribo-layers. Shuai Li et al. (Ref 24), used selective laser melting to develop Inconel 625 superalloy and a 343 HV hardness value was reported in the as-produced state. Spark plasma sintering was employed for the development of IN718 superalloy with reduced grapheme oxide reinforcement. A relative density of 92.5% and a corresponding micro-hardness value of 375 HV were obtained at the sintering temperature of 950 °C (Ref 25).

The mechanical properties such as plastic and elastic properties of materials developed via powder metallurgy techniques have been mainly influenced by inherent porosity content and their respective microstructure (Ref 26). In addition, microstructure and the properties of a material play an important role in the dynamic impact behaviour of materials and their propensity to malfunction as a result of adiabatic shear band (Ref 27). During impact, the absorbed energy is converted into internal potential energy of the system (Ref 28). Using the theory of impact, the absorbed energy can be calculated theoretically. Based on impact theory, elastic and plastic impacts are the two types of impacts. During elastic impact, there is conservation of kinetic energy throughout the process of collision or impact and the total momentum before impact or collision is equal to the momentum after impact or collision (Ref 29). Hence, the expression for energy and conservation of momentum is expressed as (Ref 29):

$$\frac{1}{2}M_A V_A^2 = \frac{1}{2}M_A V_{A2}^2 + \frac{1}{2}M_B V_{B2}^2 \quad \text{(Eq 1)}$$

$$M_A V_A = (M_A + M_B)V_0 \quad \text{(Eq 2)}$$

where $M_A$ and $M_B$ are the masses of impactor and the superalloy, respectively, while $V_A$, $V_B$ and $V_0$ are the velocities of impactor, superalloy and final velocity of the impactor and superalloy beam after collision, respectively.

Using the coefficient of restitution (e), the velocities after impact can be determined. The expression for the coefficient of restitution is given as:

$$e = \frac{V_{B2} - V_{A2}}{V_A - V_B} \quad \text{(Eq 3)}$$

The behaviour of the kinetic energy after collision is determined by the value of the coefficient of restitution. When the coefficient is close to 1, minute energy is lost and when the value is close to 0, profuse energy is lost during impact (Ref 28). The energy dissipated upon impact can be determined from the difference between the kinetic energy between the two masses after collision and impactor before collision.

$$E_{\text{Plastic}} = \frac{1}{2}M_A V_A^2 + \frac{1}{2}M_B V_B^2 - \frac{1}{2}M_{A2} V_{A2}^2 - \frac{1}{2}M_{B2} V_{B2}^2 \quad \text{(Eq 4)}$$

In this study, nickel-based superalloys were fabricated using spark plasma sintering process, which comprises of the nanostructured nickel based superalloy (NNBS) with the incorporation of milled nickel powder to nanocrystalline state and the microstrutured nickel based superalloy (MNBS), developed using the elemental powders in their as-received state. The mechanical properties which entail hardness, elastic modulus, dry sliding wear behaviour and computational predictions of their impact response were investigated.

## 2. Experimental Methodology

### 2.1 Materials

Table 1 shows the details of the elemental details of the nickel based superalloys investigated in this investigation.

### 2.2 Material Preparation and Alloy Fabrication

Nickel powder in the as-received particle size was milled to nanocrystalline size and mixed with other elemental constituents of the superalloy according to their composition to form the first alloy, denoted as Superalloy1. The nickel powder was milled via high-energy ball milling technique for 10 h at a milling speed of 350 rpm, ball-to-powder weight ratio (BPR) of 10:1, in a stainless steel pot under vacuum using ethanol as the process control agent. A nanocrystalline size of 7.9 nm after 10 h milling was obtained for the nickel powder. The experimental details of the milled nickel utilized for the preparation of the Superalloy1 has been explained in Ref. 2. The second alloy, denoted as Superalloy2, was prepared by mixing all the constituent elements according to composition in their as-received state. The mixing of the alloys was done individually for a period of 8 h in Tubular mixer to attain homogeneity prior to sintering. The mixed powders were consolidated in a graphite die in a vacuum via spark plasma sintering process (FCT System GmbH, HHPD-25) at a sintering temperature of 1100 °C, holding time of 10 min, heating rate of 100 °C/min and pressure of 50 MPa. A top mounted pyrometer positioned at 3 mm above the sample surface was used to monitor the temperature within the furnace of the SPS. Nickel-based superalloys with sample dimensions; 20-mm diameter, and 5-mm thick were sintered from SPS machine.

### 2.3 Density Evaluation

The densification behaviour of the sintered nickel-based superalloys was investigated shortly after sintering and graphite foil was removed from the surface of the sintered superalloys via sand blasting. Archimedes' principle was employed to investigate the density of the sintered nickel-based superalloys by utilizing distiled water as the immersion medium, and average of 5 measurements was recorded for each alloy to ensure consistency of values. The relative density of the sintered nickel-based superalloy was computed with respect to their theoretical density, established from the elemental mixture rule. The densification behaviour with respect to the piston displacement data gotten from the spark plasma sintering machine was also analyzed.

### 2.4 Microstructural and XRD Analysis

The sintered nickel-based superalloys samples were then subjected to mechanical polishing with a grit size of 180, up to 1-μm silicon carbide with the aid of diamond pasted. Thereafter, they were etched using a solution with the combination of 50 mL of distiled water, 10 g of $CuSO_4$, few drops of $H_2SO_4$, and 50 mL of HCl for a period of 30 s. Scanning electron microscopy (SEM, JEOLJSM-7600F) equipped with Energy Dispersive X-ray (EDX) detector was utilized to evaluate the

**Table 1 The elemental composition of nickel-based superalloy**

| Elements | Weight, % | Particle size, µm | Purity, % | Supplier |
|---|---|---|---|---|
| Chromium | 17 | 10 | 99.2 | FloMaster metal powder |
| Cobalt | 6.5 | 50 (mesh) | 99.99 | Cerac/pure advanced speciality inorganics |
| Molybdenum | 1.2 | 2.4 | 99.99 | Cerac/pure advanced speciality inorganics |
| Aluminium | 6 | 25 | 99.8 | TLS Technik GmbH and Co |
| Tungsten | 4 | 25 | 99.9 | Goodfellows |
| Tantalum | 7.6 | − 325 (mesh) | 99.9 | Aldrich chemistry |
| Nickel | Bal | 3-4 | 99.8 | Goodfellows |

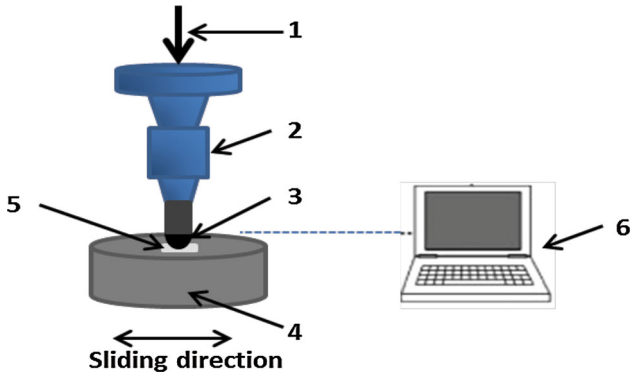


**Fig. 1** Schematic demonstration of the dry sliding wear test rig: (1) applied load; (2) load cell and carriage; (3) steel ball; (4) sintered nickel-based superalloy sample; and (5) wear scar

qualitative and quantitative elemental distribution and microstructural details of the sintered nickel-based superalloys. X-ray diffraction (XRD) with the aid of PANalytical Empyrean model with Cu Kα radiation was utilized to evaluate the phases formed in the sintered nickel-based superalloy, analyzed using Highscore plus software.

### 2.5 Mechanical and Dry Sliding Wear Test

Nanoindentation technique was employed to evaluate the indentation hardness and indentation modulus values for the sintered nickel-based superalloys from the resultant force–displacement curves using Oliver and Pharr method. This were investigated using maximum applied load of 100 mN via an Anton Paar Nanoindenter with a diamond Berkovich indenter at a 10 mN loading rate and 30 mN unloading rate. The poisson's ratio for the superalloy was fixed at 0.28.The holding time at the maximum applied load was maintained at 600 s for both superalloys. The average value of 5 indentations for each superalloy was recorded.

The dry sliding wear test was carried out using a Rtec Universal Tribometer (MFT-5000) on 20-mm diameter and 5-mm thickness superalloy samples against E52100 Alloy steel (Grade 25) of 6.35 mm diameter counter face ball at three different loads of 20, 25 and 30 N for each alloy, respectively, in accordance with ASTM-G133-05(2010) (Ref 30) standards. Cleanliness of the surfaces of the sample and the ball was done by the use of acetone before the start of the wear test, to prevent contamination of their surfaces. The test was conducted using ball-on-disc reciprocating test for 5-mm sliding distance, speed at 4 mm/s, and duration of 600 s. The wear test was conducted under unlubricated conditions at room temperatures and repeated 3 times, the frictional force, frictional coefficients ($\mu$) were monitored and wear depth recorded continuously. Figure 1 shows the schematic demonstration of the dry sliding wear test rig for the sintered nickel-based superalloys. The profile of the wear track and its related features were characterized and analysed by scanning electron microscopy (SEM) and also EDX. The wear rate of the sintered superalloys was calculated and average value was taken based on the wear volume loss ($V$) per applied load ($F$) and total sliding distance ($L$) according to the following equation (Ref 31):

$$W = V/F \cdot L\left(\mathrm{mm}^3/\mathrm{Nm}\right) \quad \text{(Eq 5)}$$

### 2.6 Finite Element Analysis (FEA) Model

The impact response of the sintered nickel-based superalloys was simulated using finite element analysis software, Abaqus CAE/2019. In the analysis, a circular shaped model of the two fabricated nickel-based superalloys with diameter 50 mm, thickness 10 mm and masses 60.7 g (Superalloy1) and 57.6 g (Superalloy2) was impacted with a rigid cylindrical impactor of diameter 20 mm, height 100 mm and total mass of 100 g. The impactor strikes the circular shaped nickel-based superalloy sample with a speed of 100 m/s in a step time of 3 ms. Dynamic explicit step with a step time of 3 ms was used because of the speed associated with impact analysis. Also, a total of 15,724 nodes and 12,882 elements consisting of 1052 linear quadrilateral elements of type R3D4 for the impactor and 11,830 linear hexagonal elements of type C3D8R for the alloy used. The developed part model for both the nickel-based superalloy and the rigid impactor is shown in Fig. 2(a) and (b), while the assembly model in Fig. 2(c).

## 3. Results and Discussions

### 3.1 Densification Behaviour

Density plays a significant role in attaining the intrinsic mechanical properties of materials developed via spark plasma sintering technique (Ref 32). This property is controlled by spark plasma sintering parameters such as the sintering temperature and time (Ref 33). After the alloys were sintered at temperature of 1100 °C, heating rate of 100 °C/min, 10 min holding time and 50 MPa, the relative density attained by the Superalloy1 and Superalloy2 were 97.29 and 92.4%, respectively.

It can be seen that the nanocrystalline nickel powder has significant effect in enhancing the relative density in the

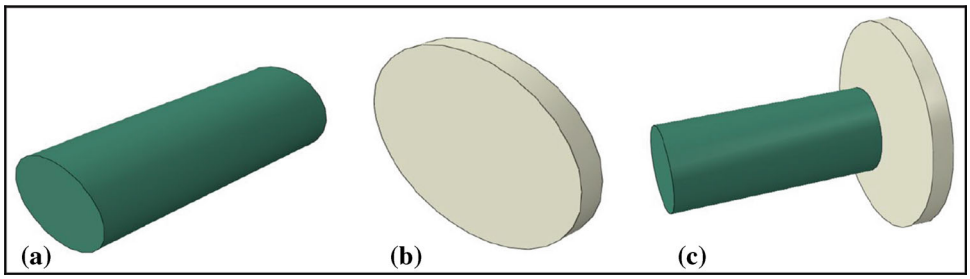


**Fig. 2** Part model for (a) impactor (b) sintered nickel-based superalloy, and (c) assembly model of impactor and superalloy

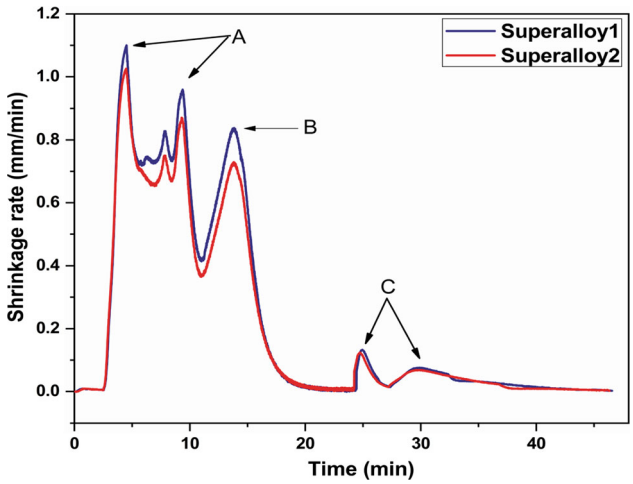


**Fig. 3** Shrinkage rate vs time of sintered nickel based superalloys as computed from the spark plasma sintering machine

Superalloy1 when compared to Superalloy2. In addition, this directly reduces the porosity in the Superalloy1 by enhancing particle parking factor. Figure 3 shows the shrinkage rate behaviour of sintered nickel based superalloys during spark plasma sintering technique. The shrinkage rate is a densification phenomenon during spark plasma sintering which depicts the displacement rate of piston movement and corresponding thickness changes of specimen. It is discovered that both sintered superalloys exhibited similar shrinkage characteristics, which shows three typical peaks (denoted by *A*, *B* and *C* in Fig. 3). However, Superalloy1 exhibited higher shrinkage behaviour than Superalloy2. This can be attributed to the presence of nanocrystalline nickel powder which increases the parking density of constituent elements in Superalloy1; this also reduces micro-porosity within the superalloy when compared to Superalloy2. The increase in shrinkage rate enhances inter-particle bonding, neck formation and growth and consequent improvement in densification and the superalloy properties. The first peak denoted by *A* is associated with initial powder particles rearrangement as a result of the application of pressure and relative movement of the punches. This followed by localized deformation at contact regions of constituents particles at the second peak (*B*), while the occurrence of bulk deformation takes place at peak *C*. This shrinkage rate behaviour is in agreement with those reported by Diouf and Molinari (Ref 34), Rominiyi et al. (Ref 32).

### 3.2 Microstructural and Phase Analysis of Sintered Nickel Based Superalloys

Figure 4(a, b) shows the SEM microscopic images of the sintered samples at a temperature of 1100 °C. As shown, the distribution of constituent elements in Superalloy1 was more homogenous than the Superalloy2. The EDX analysis confirmed the presence of the constituent elements of both alloys, and was relatively in accordance with stoichiometric compositions. EDX spot analysis was also conducted on regions denoted by 1, 2, 3 and 4 on the SEM images, and it was confirmed to be Ta, W, Cr and Ni rich regions with quantitative details presented in Table 2. The presence of porosity is lower in Superalloy1 (see Fig. 4a) when compared to Superalloy2 (Fig. 4b). This is in agreement with the densification behaviour as discussed in Sect. 3.1. The microstructural images also show the effect of sintering on inter-particle bonding, neck formation and growth of constituent particles. Enhanced inter-particle bonding, neck formation as a result of the incorporation of nanocrystalline nickel powder contributes to better densification in Superalloy1 (Ref 35).

Figure 5 shows the XRD patterns of the sintered bulk nickel-based superalloys at sintering temperature of 1100 °C. Major diffraction peaks indicate the formation of intermetallics such as $Ni_2Al_3$, $Ni_3Al$, Ni-Cr and MoNi. These are intermetallics which are often developed during the production of nickel-based superalloy with respect to elements contained by the superalloys. They exhibit excellent combination of physical and mechanical properties (Ref 36). The major peaks which represent the Ni-Cr and MoNi in Superalloy1 sample were broader when compared to the Superalloy2 sample. This effect can be attributed to the presence of nanocrystalline nickel powder. The peaks' broadening is as a result of the reduction in the crystallite size and high lattice strain during mechanical milling of nickel powder.

### 3.3 Mechanical and Dry Sliding Wear Behaviour of Spark Plasma Sintered Nickel Based Superalloys

**3.3.1 Mechanical Properties under Nanoindentation Technique.** The indentation hardness and modulus test were conducted on the sintered nickel-based alloys. Table 3 compares the indentation hardness and modulus of both sintered superalloys. It can be seen that the incorporation of nanocrystalline nickel powder enhances the indentation hardness, from 572 to 618 Hv and modulus, from 168.74 to 219.68 GPa, for Superalloy2 and Superalloy1, respectively. In addition, the maximum deformation depth recorded indicates that the Superalloy1 exhibit better resistance to deformation which corroborate the hardness value when compared to the Super-

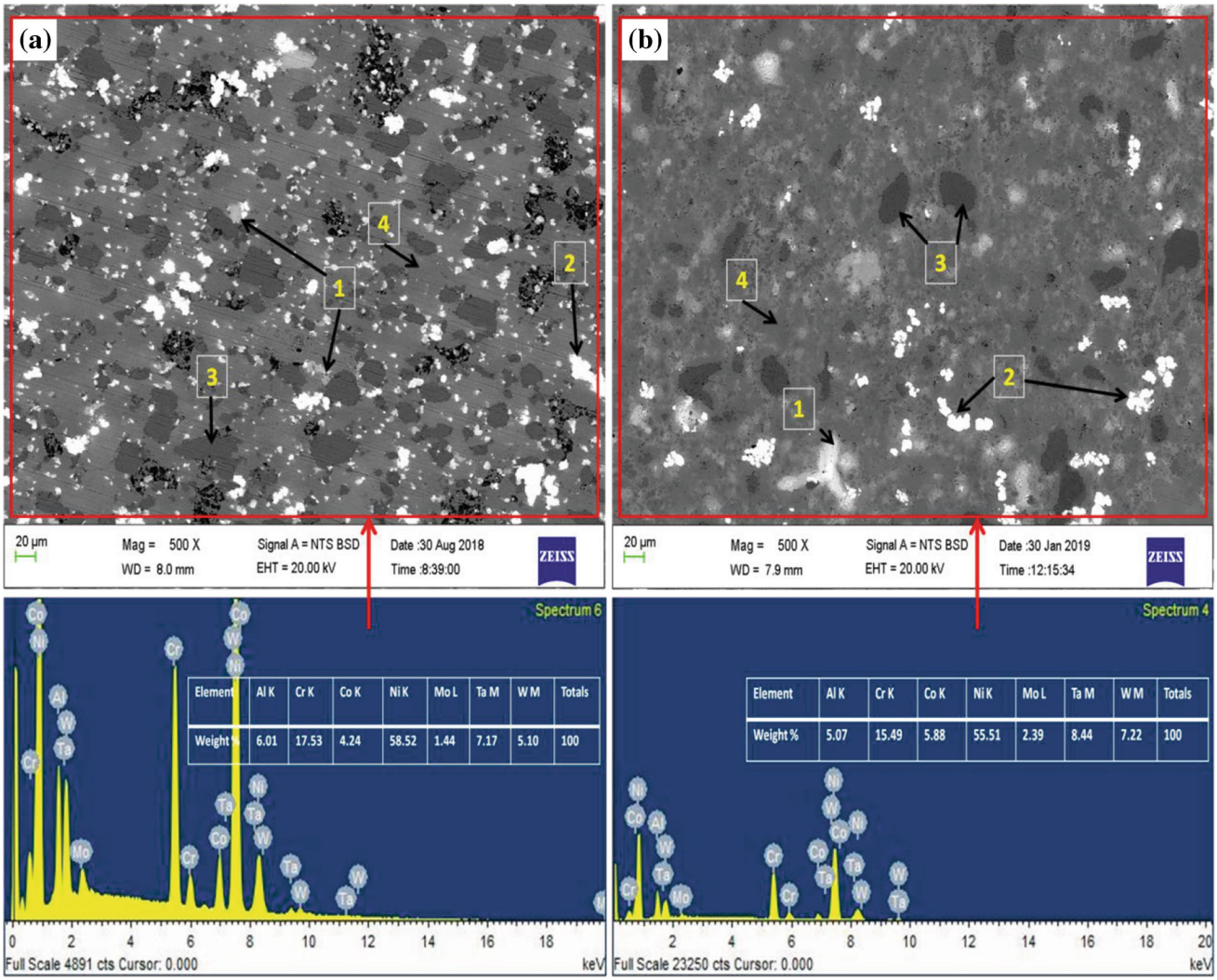


**Fig. 4** SEM images of spark plasma sintered nickel-based superalloy and EDS analysis, (a) Superalloy1 and (b) Superalloy2

**Table 2 EDX spot analysis of annotated regions in Fig. 4**

| Element, wt.% | Al K | Cr K | Co K | Ni K | Mo L | Ta M | W M | Totals |
|---|---|---|---|---|---|---|---|---|
| 1 | 0.64 | 6.06 | 0.58 | 24.74 | 0.62 | 67.36 | … | 100 |
| 2 | 1.11 | 2.95 | … | 14.56 | … | … | 81.38 | 100 |
| 3 | 0.68 | 88.60 | 1.43 | 9.29 | … | … | … | 100 |
| 4 | 6.55 | 8.66 | 1.9 | 82.08 | 0.80 | … | … | 100 |

alloy2. These are calculated from the load–displacement plot (Fig. 6) of the nickel based superalloys which also give information on the stiffness of the alloys. These results clearly indicate the role of the nanocrystalline nickel powder which plays a critical part in enhancing the mechanical property of the nickel-based superalloy due to its reduced grain size, as a result of high-energy ball milling process. This is related to the Hall–Petch relationship: The smaller the grain size, the stronger the material (Ref 37). This in agreement and can also be attributed to increased densification of nickel-based superalloy as discussed in Sect. 3.1.

The stiffness of the nickel-based superalloys, deduced from the tangent of the unloading curve of the load–displacement plot, is one of the essential properties of nickel-based superalloy (Ref 38). It can be seen that the stiffness value obtained by the Superalloy1 is higher than the Superalloy2. The presence of the nanocrystalline nickel powder which helps to increase the inter-particle bonding and indentation modulus may be attributed to enhanced stiffness of Superalloy1 when compared to Superalloy2.

**3.3.2 Dry Sliding Wear Behaviour of Sintered Nickel Based Superalloys.** The friction coefficients of the sintered nickel-based superalloys under dry sliding wear behaviour at different applied loads are presented in Fig. 7. At the initial stage of sliding which is the running in period, the coefficient of

friction increased drastically to a peak value, and at increasing sliding time, steady state behaviour of the friction coefficient was observed. The initial drastic rise in the coefficient of friction up to a peak value can be attributed to the contact of asperities present between the rubbing surfaces. The coefficient of friction of the superalloys increases with increasing applied loads. At increasing applied loads, the asperities generated between rubbing surfaces increases, and which consequently increases the frictional coefficient. During wear, asperities between surfaces can be removed as a result of friction. As a result of the removal of some of the asperities, the applied stress and wear mechanism on the worn body are influenced. This resultant change in the wear mechanism brings about the wavy pattern of the coefficient of friction (Ref 39). The Superalloy1 attains higher coefficient of friction than the Superalloy2, as shown in Fig. 7. For instance, at 30 N, the Superalloy1 attains an average coefficient of friction of 0.65, while the Superalloy2 attains 0.54. The increased coefficient of friction may be as a result of compaction and adhesion of wear debris on the surface of the superalloy which inhibit the sliding of the ball against the specimen.

Figure 8 shows the specific wear rate of the sintered nickel-based superalloys relative to the ball at different applied loads. The results show that the wear rate of the alloy increases as the applied increases, while Superalloy1 exhibit better wear resistance than Superalloy2. However, at the applied load of 30 N, higher wear rate was expected, but a decreased wear rate was observed in both sintered superalloy. The decrease in wear rate at this applied load may be attributed to the compaction of wear particles detached from the worn surface. Similar behaviour was observed by Kalyon et al. (Ref 40) on the investigation carried out on the wear behaviour of aged Inconel 718. In addition, possible formation of tribo-oxide layer formation on the wear track surface coupled with high mechanical properties such as the hardness and modulus could influence the wear resistance (Ref 23). The contact temperature between the ball and the specimen during sliding increases and this may result to the formation of tribo-oxide layer. Wang et al. (Ref 41) also attested to the fact that the presence of oxides on the specimen plays a significant role in reducing wear rate by acting as a lubricant.

In order to corroborate the wear rates of the sintered nickel based superalloys, Fig. 9 shows the wear patterns of the sintered superalloys at different applied loads. It can be seen from the images the presence worn surfaces and also compaction of wear debris. More wear compaction and exhibition of tribo-oxide were observed on Superalloy1 as shown in Fig. 9(a–c) than Superalloy2, Fig. 9(d–e). This may be attributed to the increased hardness of Superalloy1 when compared to Superalloy2. In the build up of the friction between the two alloy rubbing surfaces, the surface of the sintered superalloys become hardened and undergone considerable amount of deformation which lead to particles detaching and forming debris on the worn surface. This deformation is evident through the presence plowed and groovy features along the direction of the sliding wear, and is more noticeable at lower loads.

During sliding wear of the sintered alloy, the wear debris developed are either retained on the wear surface or displaced as loose wear debris. The retained debris continuously undergo plastic deformation, adhere to wear surface and undergo partial oxidation known as tribo-oxide layer as a result of frictional heat emanating from the continuous sliding process. Several authors have made reference to the fact that sliding friction generates heating as applied load increases (Ref 42) and as result changes the conditions of interacting surfaces (Ref 41,

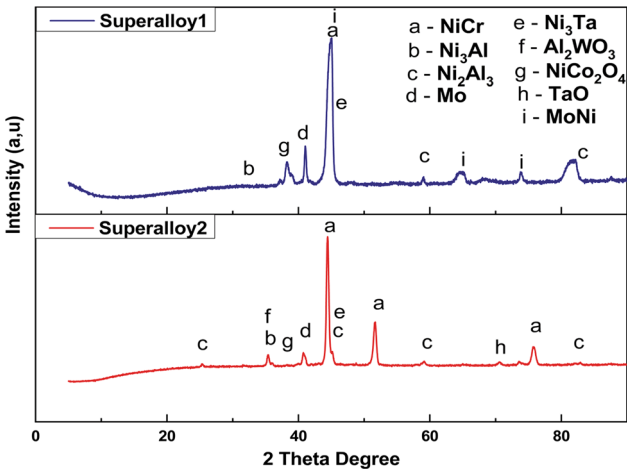


**Fig. 5** XRD pattern of spark plasma sintered nickel-based superalloys

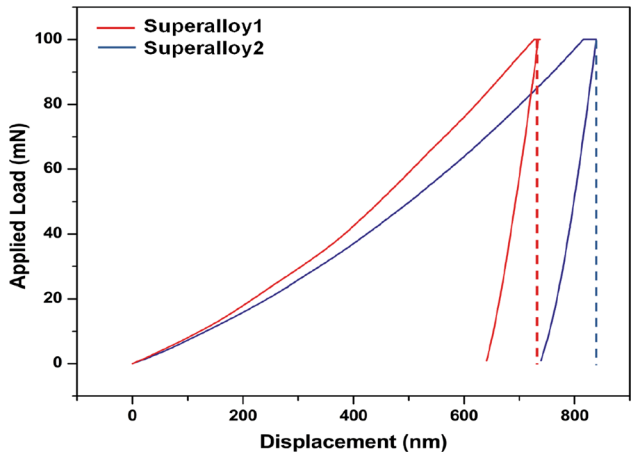


**Fig. 6** The load–displacement plot of sintered nickel-based superalloys

**Table 3 Mechanical properties of sintered nickel-based superalloys**

| Alloy | Indentaion hardness, GPa | Vickers hardness, Hv | Indentation modulus, GPa | Maximum deformation depth, nm | Stiffness, mN/nm |
|---|---|---|---|---|---|
| Superalloy2 | 6.1733 | 572 | 168.74 | 647.31 | 0.6021 |
| Superalloy1 | 6.677 | 618 | 219.68 | 834.84 | 0.7144 |

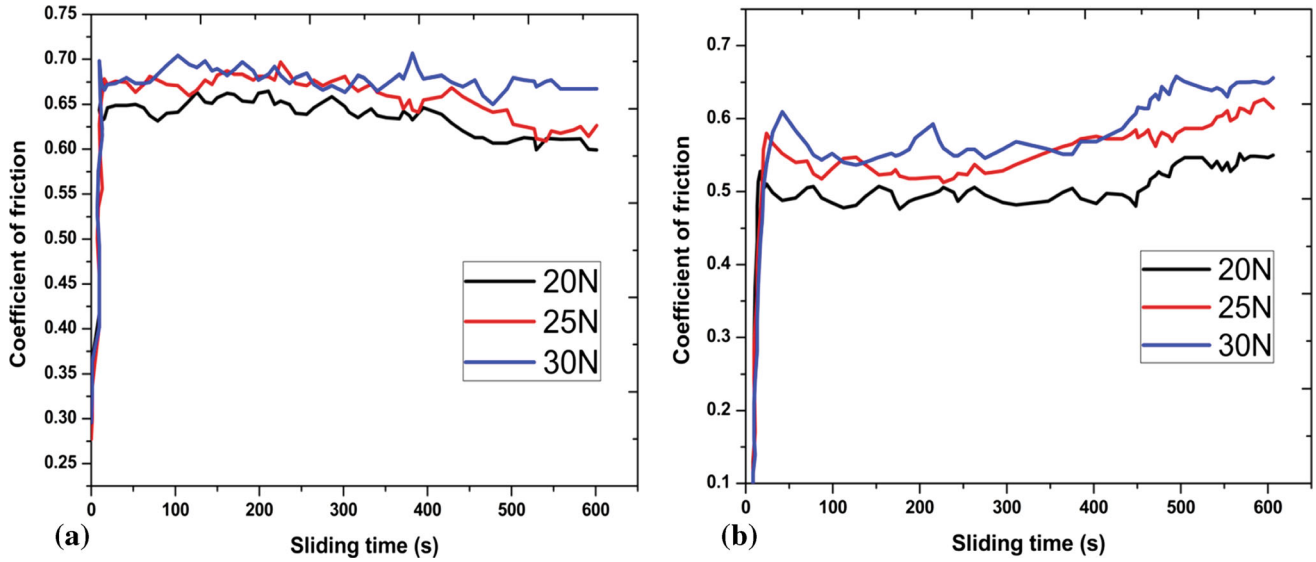


**Fig. 7** The coefficient of friction against sliding time (s) at different applied loads; (a) Superalloy1, and (b) Superalloy2

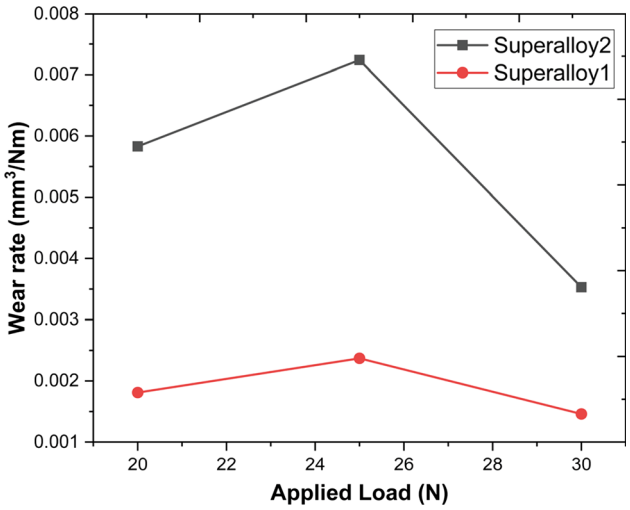


**Fig. 8** The effect of applied loads on the wear rate of the sintered nickel-based superalloys

43). This development of tribo-oxide layer gain more effect at higher applied loads (as reflected in Fig. 9) and helps to protect the sub surface of the superalloy from further wear activities (Ref 43). The tribo-layers were further analyzed using EDS analysis at points 1 and 2 in Fig. 9(c) and (f), respectively, and are presented in Fig. 10. The EDS analysis indicates the traces of Fe particles, this may imply that part of the ball wear off during the process. However, there are more of these Fe particles during the sliding wear process of Superalloy1 than the Superalloy2 as indicated by the EDS quantitative chart embedded in Fig. 10. These corroborate the superior hardness of Superalloy1 over Superalloy2.

The features exhibited by the sintered superalloys in the worn surface morphologies at different applied loads (Fig. 9) helps to reveal their wear mechanisms. The wear mechanisms are characterized by both abrasive and adhesive wear. In both alloys, at lower applied loads, grooves and plowed surfaces as a result of deformation and removal of wear debris were observed which is characteristic of abrasive wear. This features changes as the applied load increases, more compaction of retained wear debris were observed on the worn surfaces of the superalloys which indicate an adhesive wear.

### 3.4 High Velocity Impact Response Simulation Analysis

The graph for the mesh convergence study conducted by gradually reducing the global seed size until a suitable mesh size that gives an accurate result with a reasonable computational time is shown in Fig. 11(a) and the impactor-alloy assembly mesh is depicted in Fig. 11(b). From the study, mesh size of 2 mm with a total of 11,882 elements was found suitable for the analysis.

The stress developed on the in both the Superalloy2 and Superalloy1 is shown in Fig. 12(a) and (b), respectively. After impact, the stress developed on Superalloy1 is higher than that developed in the Superalloy2. The reason for the increase in the stress developed on Superalloy1 can be attributed to the grain size of the particles in the alloy, since the stress developed in a material decreases with increase in grain size.

The elastic and plastic strain experienced by both superalloys are depicted in Fig. 13. Both the elastic and plastic strain developed in the Superalloy2 is lower than that developed on Superalloy1 upon impact. The value of both strains is an indication that the Superalloy1 is more ductile and thus, will undergo extensive plastic deformation prior to failure as compared to the Superalloy2.

As depicted in Fig. 14(a) and (b), the displacement experienced by Superalloy1 is higher than that experienced by Superalloy2 upon impact. The higher displacement experienced by the Superalloy1 can be attributed to it higher rigidity as compared to that of the Superalloy2.

The total strain energy absorbed by the superalloys was computed by Abaqus using the strain energy equation, while the absorbed kinetic energy was computed using Eq 4. It was observed that the Superalloy1 proved its superiority in the area of energy absorption as it absorbs more energy upon impact. This behaviour of the Superalloy1 can also be attributed to enhanced particle bonding which exist within its structure. Figure 15(a) and (b) shows the graph for the kinetic and total strain energy absorbed by the superalloys. From the graph, it

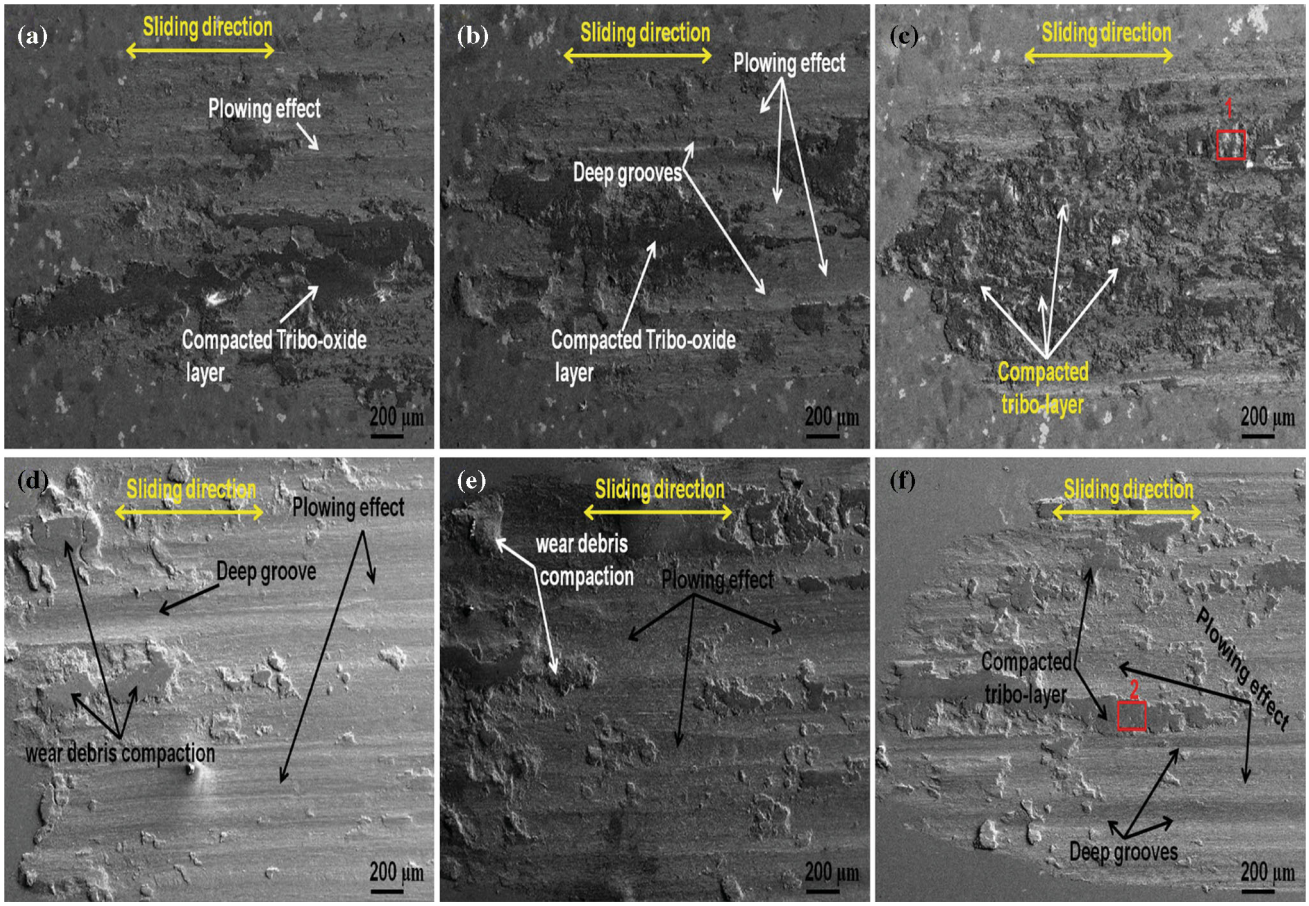


**Fig. 9** SEM images of wear tracks of Superalloy1 at; (a) 20 N, (b) 25 N, (c) 30 N, and Superalloy2 at;(d) 20 N, (e) 25 N, and (f) 30 N applied loads

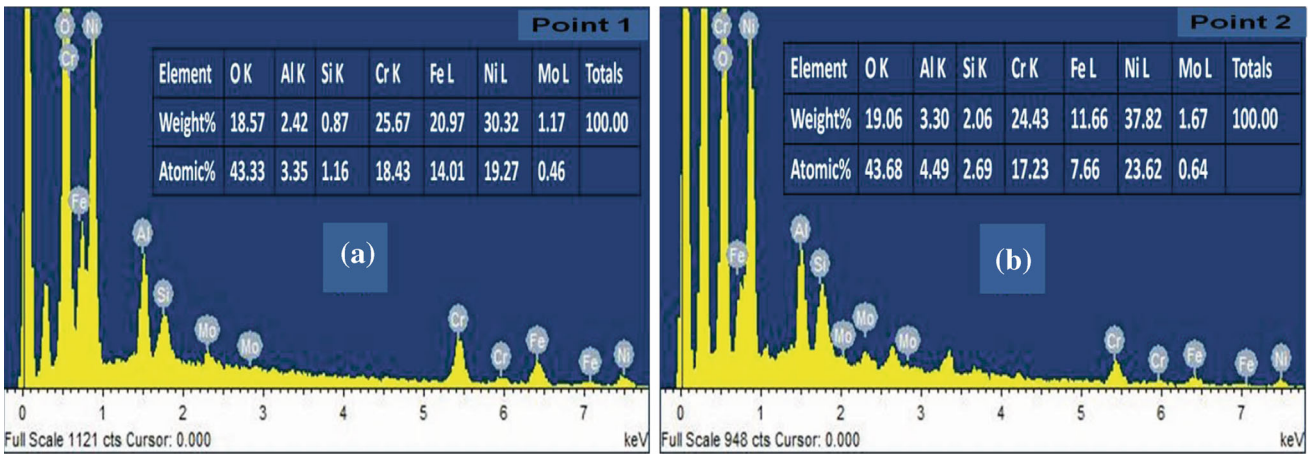


**Fig. 10** EDS analysis for spot analysis for (a) Superalloy1 as indicated on Fig. 8c, and (b) Superalloy2 as indicated on Fig. 9f

was observed that both superalloys attained their maximum total strain and kinetic energy at the same step time after impact. However, the value of the strain energy in Superalloy1 is higher than that of the Superalloy2. Also, the strain and kinetic energies in both superalloys were observed to decrease with increase in step time.

## 4. Conclusion

A study of the effect high-energy ball milling on the mechanical, dry sliding wear behaviour and high velocity impact response of sintered nickel-based superalloys, namely Superalloy1 and Superalloy2 were studied in this work. The following are the conclusions drawn from the study.

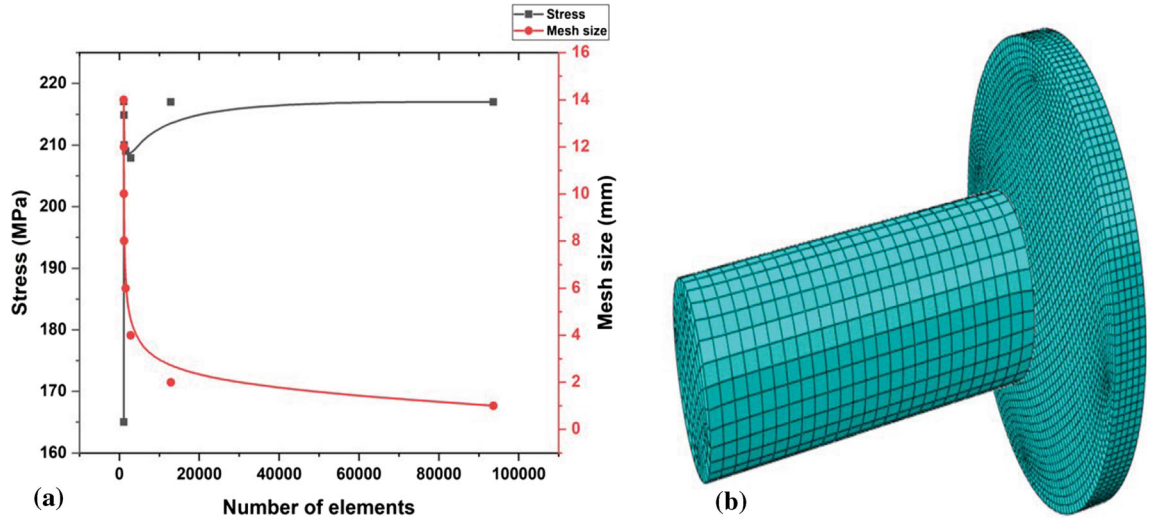


**Fig. 11** (a) Meshed study graph and (b) assembly mesh of impactor and superalloy

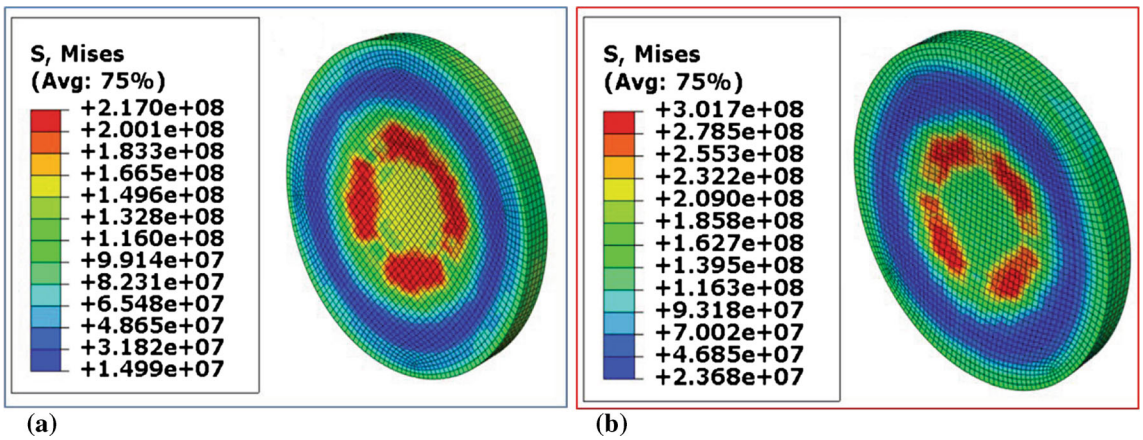


**Fig. 12** Contour plot for stress developed in (a) Superalloy2 and (b) Superalloy1

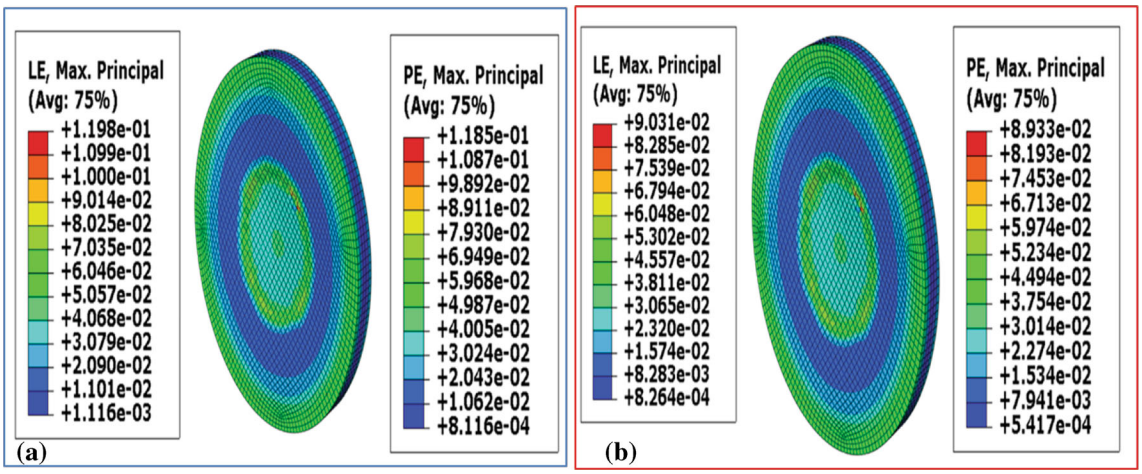


**Fig. 13** Contour plot for Elastic Strain (LE) and Plastic Strain (PE) developed in (a) Superalloy2, and (b) Superalloy1

The incorporation of nanocrystalline nickel powder developed via high-energy ball milling in the Superalloy1 enhances the hardness value. This is evident through higher densification and indentation hardness values observed, which is higher than the Superalloy2.

The wear rate of the alloys increases as the applied load increases, but reduction in the wear rate at the maximum load applied was observed in both sintered superalloys. This is attributed to the formation of tribo-oxide layer formation arising from retained wear debris on the worn surface.

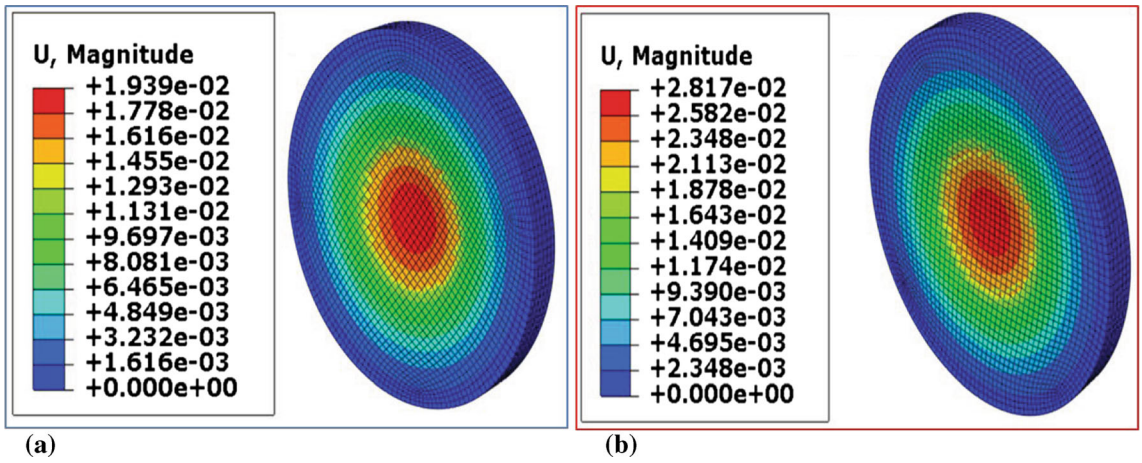


**Fig. 14** Contour plot for displacement in (a) Superalloy2 and (b) Superalloy1

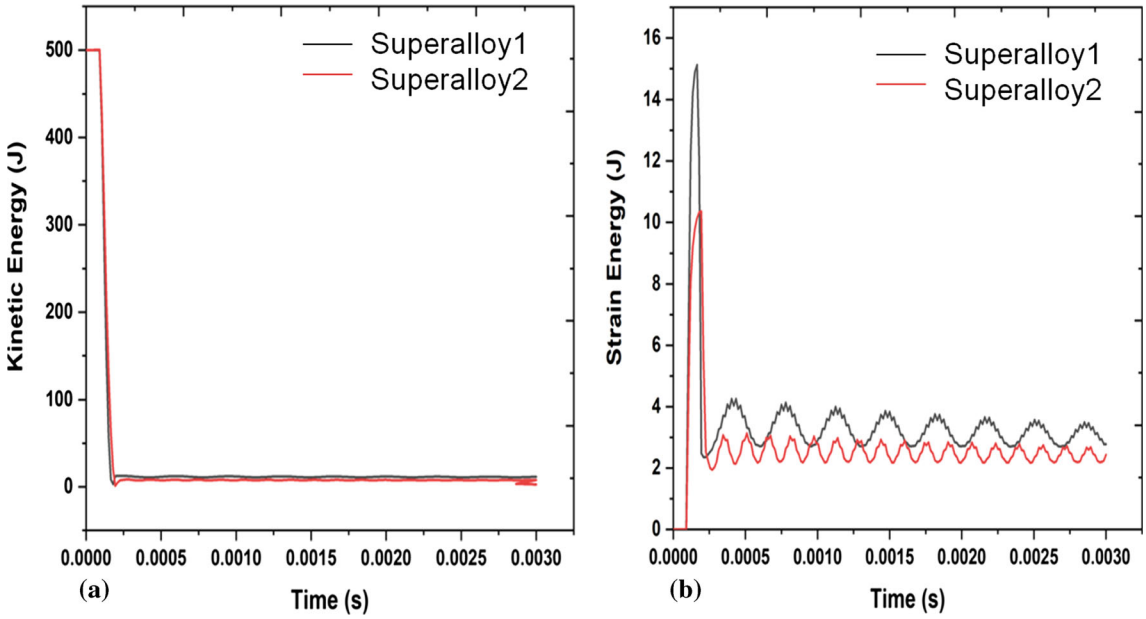


**Fig. 15** Graph of (a) kinetic energy and (b) total strain energy developed in both sintered nickel-based superalloy

Notwithstanding, the Superalloy1 exhibits better wear resistance properties than Superalloy2.

High velocity impact response of Superalloy2 and Superalloy1 simulated in finite element analysis software, Abaqus indicates that the stress developed in Superalloy1 is higher than that developed in Superalloy2. The reason for this increase is attributed to the smaller grain size of the Superalloy1.

The elastic and plastic strain developed in the Superalloy2 is lower than that developed in the Superalloy1. Thus, signifying that Superalloy1 has higher ductility and will undergo extensive plastic deformation prior to failure during operation. Lastly, the Superalloy1 has higher energy absorption capability ability than the microstructure due to its ability to endure extensive plastic deformation before failure.

## Acknowledgments

Research facilities supported by the Institute for NanoEngineering Research, Tshwane University of Technology, and Centre for Nanomechanics and Tribocorrosion, School of Mining, Metallurgical and Chemical Engineering, University of Johannesburg 2028, South Africa.

## Funding

National Research Foundation of South Africa.

## References

1. O. Palavar, D. Özyürek, and A. Kalyon, Artificial Neural Network Prediction of Aging Effects on the Wear Behavior of IN706 Superalloy, *Mater. Des.*, 2015, **82**, p 164–172
2. B.J. Babalola, M.B. Shongwe, A.L. Rominiyi, S.O. Jeje, and P.A. Olubambi, A Study of Nanocrystalline Nickel Powders Developed Via High-energy Ball Milling, *Int. J. Adv. Manuf. Technol.*, 2019, **102**, p 3657–3665
3. J. Sheng, S. Huang, J.Z. Zhou, and Z.W. Wang, Effects of Warm Laser Peening on the Elevated Temperature Tensile Properties and Fracture

Behavior of IN718 Nickel-Based Superalloy, *Eng. Fract. Mech.*, 2017, **169**, p 99–108
4. B.J. Babalola, N. Maledi, M.B. Shongwe, M.O. Bodunrin, B.A. Obadele, and P.A. Olubambi, Influence of Nanocrystalline Nickel Powder on Oxidation Resistance of Spark Plasma Sintered Ni-17Cr6.5Co1.2Mo6Al4W7.6Ta Alloy, *J. King Saud Univ. Eng. Sci.*, 2019, **32**, p 198–204
5. H. Zhang, H. Zhou, S. Qin, J. Liu, and X. Xu, Effect of Deformation Parameters on Twinning Evolution During Hot Deformation in a Typical Nickel-Based Superalloy, *Mater. Sci. Eng., A*, 2017, **696**, p 290–298
6. B.J. Babalola, M.B. Shongwe, B.A. Obadele, and P.A. Olubambi, Densification, Microstructure and Mechanical Properties of Spark Plasma Sintered Ni-17%Cr Binary Alloys, *Int. J. Adv. Manuf. Technol.*, 2018, **101**, p 8
7. B.J. Babalola, M. Shongwe, A. Rominiyi, and P. Lepele, The Fabrication and Characterization of Spark Plasma Sintered Nickel Based Binary Alloy at Different Heating Rate. *J. Micro and Nano-Manuf.*, 2019, **7**, p 031004
8. C. Sommitsch, R. Radis, A. Krumphals, M. Stockinger, and D. Huber, 12-Microstructure Control in Processing Nickel, Titanium and Other Special Alloys, *Microstructure Evolution in Metal Forming Processes*, J. Lin, D. Balint, and M. Pietrzyk, Ed., Woodhead Publishing, Cambridge, 2012, p 337–383
9. K. Dash, D. Chaira, and B.C. Ray, Synthesis and Characterization of Aluminium-Alumina Micro- and Nano-composites by Spark Plasma Sintering, *Mater. Res. Bull.*, 2013, **48**, p 2535–2542
10. B.M. Moshtaghioun, F.L. Cumbrera-Hernández, D. Gómez-García, S. de Bernardi-Martín, A. Domínguez-Rodríguez, A. Monshi et al., Effect of Spark Plasma Sintering Parameters on Microstructure and Room-Temperature Hardness and Toughness of Fine-Grained Boron Carbide (B4C), *J. Eur. Ceram. Soc.*, 2013, **33**, p 361–369
11. K. Sairam, J.K. Sonber, T.S.R.C. Murthy, C. Subramanian, R.K. Fotedar, P. Nanekar et al., Influence of Spark Plasma Sintering Parameters on Densification and Mechanical Properties of Boron Carbide, *Int. J. Refract Metal Hard Mater.*, 2014, **42**, p 185–192
12. R. Licheri, C. Musa, R. Orrù, G. Cao, D. Sciti, and L. Silvestroni, Bulk Monolithic Zirconium and Tantalum Diborides by Reactive and Non-reactive Spark Plasma Sintering, *J. Alloys Compd.*, 2016, **663**, p 351–359
13. E. Serrano-Pérez, H. Martinez-Gutierrez, K.J. Martinez-Gonzalez, E. Marín-Moares, and F. Juárez-López, Densification and Microstructure of Spark Plasma Sintered 7YSZ–Gd2O3 Ceramic Nano-Composites, *J. Asian Ceram. Soc.*, 2017, **5**, p 266–275
14. X. Yang, X. Wang, P. Wang, K. Hu, Z. Li, and J. Zhang, Spark Plasma Sintering of SiC-LaB6 Composite, *J. Alloys Compd.*, 2017, **704**, p 329–335
15. B.J. Babalola, M.B. Shongwe, B.A. Obadele, P.A. Olubambi, O.O. Ayodele, A.L. Rominiyi et al., Comparative Study of Spark Plasma Sintering Features on the Densification of Ni-Cr Binary Alloys, *MATEC Web Conf.*, 2018, **249**, p 01004
16. Y.J. Wu, J. Li, X.M. Chen, and K. Kakegawa, Densification and Microstructures of PbTiO3 Ceramics Prepared by Spark Plasma Sintering, *Mater. Sci. Eng., A*, 2010, **527**, p 5157–5160
17. F. Ye, Z. Hou, H. Zhang, L. Liu, and Y. Zhou, Spark Plasma Sintering of cBN/β-SiAlON Composites, *Mater. Sci. Eng., A*, 2010, **527**, p 4723–4726
18. R. Orrù, R. Licheri, A.M. Locci, A. Cincotti, and G. Cao, Consolidation/Synthesis of Materials by Electric Current Activated/Assisted Sintering, *Mater. Sci. Eng. R Rep.*, 2009, **63**, p 127–287
19. M.M. Tünçay, J.A. Muñiz-Lerma, D.P. Bishop, and M. Brochu, Spark Plasma Sintering and Spark Plasma Upsetting of an Al-Zn-Mg-Cu Alloy, *Mater. Sci. Eng. A*, 2017, **704**, p 154–163
20. A. Thakur and S. Gangopadhyay, State-of-the-art in Surface Integrity in Machining of Nickel-Based Super Alloys, *Int. J. Mach. Tools Manuf.*, 2016, **100**, p 25–54
21. K. Thirugnanasambantham and S. Natarajan, Mechanistic Studies on Degradation in Sliding Wear Behavior of IN718 and Hastelloy X Superalloys at 500 °C, *Tribol. Int.*, 2016, **101**, p 324–330
22. Y. Ustinovshikov, Formation of Microstructures Responsible for Remarkable Properties of the Ni-and Co-Based Superalloys, *Acta Mater.*, 2016, **111**, p 66–74
23. Y. Gao and M. Zhou, Superior Mechanical Behavior and Fretting Wear Resistance of 3D-Printed Inconel 625 Superalloy, *Appl. Sci.*, 2018, **8**, p 2439
24. S. Li, Q. Wei, Y. Shi, Z. Zhu, and D. Zhang, Microstructure Characteristics of Inconel 625 Superalloy Manufactured by Selective Laser Melting, *J. Mater. Sci. Technol.*, 2015, **31**, p 946–952
25. S. Ma, Y. Yang, A. Li, S. Zhou, L. Shi, S. Wang et al., Effects of Temperature on Microstructure and Mechanical Properties of IN718 Reinforced by Reduced Graphene Oxide Through Spark Plasma Sintering, *J. Alloys Compd.*, 2018, **767**, p 675–681
26. S.Z. Chavoshi, V.L. Tagarielli, Z. Shi, J. Lin, S. Wang, J. Jiang et al., Predictions of the Mechanical Response of Sintered FGH96 Powder Compacts, *J. Eng. Mater. Technol.*, 2020, **142**, p 1–23
27. G. Asala, J. Andersson, and O. Ojo, A Study of the Dynamic Impact Behaviour of IN 718 and ATI, 718Plus® Superalloys, *Philos. Mag.*, 2019, **99**, p 419–437
28. S. Muhammad Nasiruddin, A. Hambali, J. Rosidah, W. Widodo, and M. Ahmad, A Review of Energy Absorption of Automotive Bumper Beam, *Int. J. Appl. Eng. Res.*, 2017, **12**, p 238–245
29. S. Salifu, D. Desai, O. Ogunbiyi, R. Sadiku, O. Adesina, and O. J. M. T. P. Adesina, Comparative Study of High Velocity Impact Response of Aluminium 3105-H18 and Carbon Fibre-Epoxy Composite Double Hat Bumper Beams. *Mater. Today: Proc.*, 2020. https://doi.org/10.1016/j.matpr.2020.03.828
30. ASTM Standard G133-05. *Standard Test Method for Linearly Reciprocating Ball-on-Flat Sliding Wear,* Annual Book of ASTM Standards, vol. 03.02, 2010
31. S.O. Jeje, M.B. Shongwe, E.N. Ogunmuyiwa, A.L. Rominiyi, and P.A. Olubambi, Microstructure, Hardness, and Wear Assessment of Spark-Plasma-Sintered Ti-xAl-1Mo Alloy, *Metall. Mater. Trans. A*, 2020, **51**, p 4033–4044
32. A.L. Rominiyi, M.B. Shongwe, N. Maledi, B.J. Babalola, and P.A. Olubambi, Synthesis, Microstructural and Phase Evolution in Ti–2Ni and Ti–10Ni Binary Alloys Consolidated by Spark Plasma Sintering Technique, *Int. J. Adv. Manuf. Technol.*, 2019, **104**, p 1041–1049
33. A. Khalil, A. S. Hakeem, and N. Saheb, Optimization of Process Parameters in Spark Plasma Sintering Al6061 and Al2124 Aluminum Alloys, in *Advanced Materials Research* (2011), pp. 1517–1522
34. S. Diouf and A. Molinari, Densification Mechanisms in Spark Plasma Sintering: Effect of Particle Size and Pressure, *Powder Technol.*, 2012, **221**, p 220–227
35. M.B. Shongwe, S. Diouf, M.O. Durowoju, and P.A. Olubambi, Effect of Sintering Temperature on the Microstructure and Mechanical Properties of Fe–30%Ni Alloys Produced by Spark Plasma Sintering, *J. Alloys Compd.*, 2015, **649**, p 824–832
36. M. Krasnowski, S. Gierlotka, S. Ciołek, and T. Kulik, Nanocrystalline NiAl Intermetallic Alloy with High Hardness Produced by Mechanical Alloying and Hot-Pressing Consolidation, *Adv. Powder Technol.*, 2019, **30**, p 1312–1318
37. A. Olayinka, W.J. Emblom, T.C. Pasacreta, and S.W. Wagner, The Effect of Hydraulic Bulge Process on the Surface Topography of Annealed AISI, 304 Stainless Steel, *Proc. Manuf.*, 2017, **10**, p 243–252
38. M. McLean, "Nickel-Based Alloys: Recent Developments for the Aero-Gas Turbine," in *High Performance Materials in Aerospace* (Springer, 1995), pp. 135–154
39. K. Thirugnanasambantham, R. Raju, T. Sankaramoorthy, P. Velmurugan, A. Kannagi, M. Chaitanya Kishore Reddy et al., Degradation Mechanism for High-Temperature Sliding Wear in Surface-Modified In718 Superalloy, *Cogent Eng.*, 2018, **5**, p 1501864
40. A. Kalyon, O. Palavar, and D. Özyürek, An Investigation of the Wear Performance of Aged Inconel 718 Superalloy by the Fuzzy Logic Approach, *J. Mater. Eng. Perform.*, 2019, **28**, p 2853–2865
41. Y. Wang, S. Zhao, Z. Jia, J. Ji, D. Liu, T. Guo, et al., Study on Friction and Wear Behavior of Inconel 625 Superalloy during Hot Extrusion, *Adv. Mater. Sci. Eng.* 2020. https://doi.org/10.1155/2020/5453703
42. R.A. Al-Samarai, A.K. Haftirman, and Y. Al-Douri, Effect of Load and Sliding Speed on Wear and Friction of Aluminum-Silicon Casting Alloy, *Int. J. Sci. Res. Publ.*, 2012, **2**, p 1–4
43. S. Mishra, K. Chandra, and S. Prakash, Dry Sliding Wear Behaviour of Nickel-, Iron-and Cobalt-Based Superalloys, *Tribol. Mater. Surfaces Interfaces*, 2013, **7**, p 122–128